Journal of Solid State Chemistry 183 (2010) 2589–2597

Contents lists available at ScienceDirect

Journal of Solid State Chemistry

journal homepage: www.elsevier.com/locate/jssc

Synthesis, structural characterization and Li^+ ion conductivity of a new vanado-molybdate phase, $LiMg_3VMo_2O_{12}$

Lisa J. Gillie [a,*], Sharon A. de Souza [b], Denis Sheptyakov [c], Nik Reeves-McLaren [b], Denis Pasero [b], Anthony R. West [b]

[a] Department of Chemical and Biological Sciences, School of Applied Sciences, University of Huddersfield, Queensgate, Huddersfield HD1 3DH, UK
[b] Department of Engineering Materials, Sir Robert Hadfield Building, University of Sheffield, Mappin Street, Sheffield S1 3JD, UK
[c] Laboratory for Neutron Scattering, ETHZ&PSI, CH-5232 Villigen PSI, Switzerland

ARTICLE INFO

Article history:
Received 5 July 2010
Received in revised form
27 August 2010
Accepted 31 August 2010
Available online 8 September 2010

Keywords:
3D framework compounds
Lithium molybdate
Neutron diffraction
Impedance spectroscopy
Ionic conductivity
Cation ordering

ABSTRACT

A new vanado-molybdate $LiMg_3VMo_2O_{12}$ has been synthesized, the crystal structure determined an ionic conductivity measured. The solid solution $Li_{2-z}Mg_{2+z}V_zMo_{3-z}O_{12}$ was investigated and the structures of the $z=0.5$ and 1.0 compositions were refined by Rietveld analysis of powder X-ray (XRD) and powder neutron diffraction (ND) data. The structures were refined in the orthorhombic space group *Pnma* with $a\sim5.10$, $b\sim10.4$ and $c\sim17.6$ Å, and are isostructural with the previously reported double molybdates $Li_2M_2(MoO_4)_3$ ($M=M^{2+}$, $z=0$). The structures comprise of two unique $(Li/Mg)O_6$ octahedra, $(Li/Mg)O_6$ trigonal prisms and two unique $(Mo/V)O_4$ tetrahedra. A well-defined 1:3 ratio of Li^+:Mg^{2+} is observed in octahedral chains for $LiMg_3VMo_2O_{12}$. Li^+ preferentially occupies trigonal prisms and Mg^{2+} favours octahedral sheets. Excess V^{5+} adjacent to the octahedral sheets may indicate short-range order. Ionic conductivity measured by impedance spectroscopy (IS) and differential scanning calorimetry (DSC) measurements show the presence of a phase transition, at 500–600 °C, depending on *x*. A decrease in activation energy for Li^+ ion conductivity occurs at the phase transition and the high temperature structure is a good Li^+ ion conductor, with $\sigma=1\times10^{-3}$–4×10^{-2} S cm^{-1} and $E_a=0.6$ to 0.8 eV.

1. Introduction

Inorganic structures of mixed metal oxides containing discrete $(V,Mo)O_4$ tetrahedra have been intensively studied due to industrial demand for the selective oxidative dehydrogenation (ODH) of light hydrocarbons in the petrochemical industry [1–4]. Traditionally, spinel-related phases such as $Mg_3V_2O_8$ are used for ODH, but explorations into phase relations in the Mg–V–Mo–O system resulted in the discovery of a new vanado-molybdate, $Mg_{2.5}VMoO_8$, [5,6] which has comparable catalytic properties to $Mg_3V_2O_8$ [7]. This material has a 3D-framework structure, constructed of five different metal-oxygen coordination polyhedra (Fig. 1). Hexagonal tunnels are formed from buckled sheets of edge- and corner-sharing MgO_6 octahedra linked by edge-sharing chains of MgO_6 trigonal prisms. Chains of face-sharing MgO_6 octahedra run parallel to these tunnels and are tethered to the main framework by isolated $(Mo,V)O_4$ tetrahedra. Some cation vacancies are located in the face-sharing octahedral chains. Structural analogues of these frameworks were first reported in the 1970s [8–17] and were referred to as "double molybdates" of general formula $A^+_{2m}M^{2+}_n(MoO_4)_{m+n}$: A=Li, Na, K or Ag; B=Mg, Zn, Mn, Ni or Co [8–15,17,18 and references therein]. Relevant to this paper are several examples where A=Li [9,15,17–19]. In the $Li_2M_2(MoO_4)_3$ family, there are no cation vacancies in the octahedral chains and the three 6-coordinate sites contain a mixture of Li^+ and M^{2+} ions.

Alkali-containing framework structures in general have attracted great interest over the last few decades, principally for their ionic conducting properties, and hence, their use as solid electrolytes [20–22]. A prominent example is NASICON, a non-redox active sodium zirconium silicophosphate [20]. The structural framework is built from $(Si,P)O_4$ tetrahedra and ZrO_6 units linked to produce a relatively open 3D network of sites with conduction pathways for the mobile Na^+ cations. NASICON exhibits a similar structure to the double molybdates; however, the connectivity of the polyhedra is slightly different. The unlithiated framework structure $Fe_2(MoO_4)_3$ can reversibly intercalate lithium to form a metastable orthorhombic structure (*Pbcn*), α-$Li_2Fe_2(MoO_4)_3$, which undergoes an irreversible phase transformation at higher temperatures to form stable orthorhombic β-$Li_2Fe_2(MoO_4)_3$, isostructural with the double molybdates [22]. In the unlithiated α-form, all polyhedra are connected

* Corresponding author. Fax: +44 1484 472182.
E-mail address: L.J.Gillie@hud.ac.uk (L.J. Gillie).

0022-4596/$ - see front matter © 2010 Elsevier Inc. All rights reserved.
doi:10.1016/j.jssc.2010.08.042

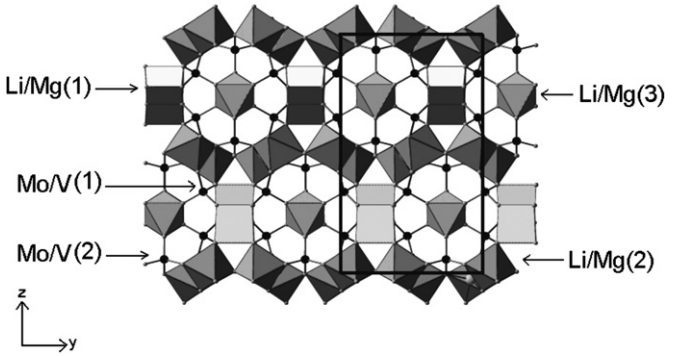

Fig. 1. Crystal structure of $Mg_{2.5}VMoO_8$ and $Li_{2-z}Mg_{2+z}V_zM_{3-z}O_{12}$.

via corners; upon intercalation, lithium is accommodated in distorted tetrahedral sites formed by the edges of two distorted FeO_6 octahedra [23,24]. Both α- and β-forms are of interest for their Li^+ ion conductivity; however, a more open network of polyhedra is present in the α-form than in the β-form, which comprises several edge-, corner- and face-sharing polyhedra.

The reversible deintercalation of mobile Li^+ ions is possible in several structure types, leading to applications as electrodes in rechargeable lithium batteries, provided the component structural framework and mobile cations exhibit the required redox and conductivity behaviour, respectively. $LiNiVO_4$ exhibits an inverse spinel structure and is a potential candidate for positive electrodes in rechargeable Li^+ ion battery systems [25]. Li^+ ions can be reversibly deintercalated at a potential of ca. 4.8 V (vs. Li-metal anode) with a theoretical capacity of 148 mA h/g [25]. We attempted to synthesize new structural analogues by doping $LiNiVO_4$ according to: $Li^+ + V^{5+} \Leftrightarrow Mo^{6+}$; this resulted in phase mixtures of the inverse spinel and an unknown phase, which showed a remarkable similarity to $M_{2.5}VMoO_8$ (M=Mg, Zn, Mn, Co) [6,26] and double molybdate families of phases. Similar investigation into the Mg system revealed a new vanado-molybdate phase $LiMg_3VMo_2O_{12}$, and a solid solution between this and $Li_2Mg_2(MoO_4)_3$. These are interesting not only from a crystallographic perspective, but also as potential host structures for either Li^+ ion conductivity or mixed Li^+/e^- conductivity.

There are no previous reports of Li-containing divalent metal vanado-molybdates, but some studies on the electrical properties of the double molybdates have been conducted [15,27–28]. The highest Li^+ ion conductivity is generally observed for frameworks in which the trigonal prismatic sites contain exclusively lithium. Recent studies of $Li_2M_2(MoO_4)_3$ (M=Ni, Co), their electrochemical activity and properties as cathode materials have been reported [29,30]. We report here the synthesis, structure and properties of a new vanado-molybdate phase $LiMg_3VMo_2O_{12}$, and solid solutions on the $Li_2Mg_2Mo_3O_{12}$—$LiMg_3VMo_2O_{12}$ join, which form by the double substitution mechanism: $Li^+ + Mo^{6+} \Leftrightarrow V^{5+} + Mg^{2+}$; this work forms part of a larger investigation into the quaternary systems of Li_2O–$M^{2+}O$–V_2O_5–MoO_3 (M=Zn, Mg, Ni, Co, Mn). Some of the simple relations of $LiMg_3VMo_2O_{12}$ to other well known phases in the system are described below. $Mg_{2.5}VMoO_8$ and the hypothetical composition $Mg_4V_2MoO_{12}$ (which is actually a mixture of $Mg_3V_2O_8$ and $Mg_{2.5}VMoO_8$) lie along the $Mg_3V_2O_8$–$MgMoO_4$ join in the ternary system. The z=1 phase reported here is located on the $Li_2Mg_2Mo_3O_{12}$–$Mg_4V_2MoO_{12}$ join, which intersects the line between $MgMoO_4$ and $LiMgVO_4$ at the z=1 composition. Compositions with values of z up to 2 were synthesized, however a solid solution was only formed up to z=1.

2. Experimental

Polycrystalline $Li_{2-z}Mg_{2+z}V_zMo_{3-z}O_{12}$ samples were synthesized by standard ceramic techniques from stoichiometric proportions of reagent grade Li_2CO_3, MgO, V_2O_5 and $(NH_4)_2MoO_4$. The mixtures were ground using an agate pestle and mortar using acetone as a homogenizing medium, the powders transferred to gold foil boats and initially fired in air up to 500–600 °C. The temperature was increased slowly over a period of several days until single-phase products were achieved. As z increased, the firing temperature was raised accordingly (625 °C, 3 days for z=0; 800 °C, 2 days for z=0.5; 925 °C, 1 day for z=1).

Phase purity was verified by powder X-ray diffraction (XRD) and profiles were compared with reported isostructural phases on the Joint Committee of Powder Diffraction Standards (JCPDS) database [31]. Data suitable for structural analysis were collected on a Stoe STADI P diffractometer ($CuK\alpha_1$ radiation; 1.54059 Å). Powder neutron diffraction (ND) data were collected on the high resolution powder diffractometer, HRPT at SINQ (PSI, Switzerland) at both ambient temperature and at 650 °C, λ=1.494 Å. Samples were sealed in vanadium canisters for ambient temperature measurements and stainless steel canisters for high temperature measurements. Data were corrected for absorption using an in-house procedure and the FOX programme [32] was used for the investigation of the validity of the initial refinement model by *ab initio* structure determination. The resultant model was used as the starting point for joint XRD/ND Rietveld refinements, performed using the GSAS suite of programmes [33].

For impedance measurements, powders were pressed into cylindrical discs under a pressure of 0.5–1.0 tonnes and sintered at various temperatures and times, depending on composition. Pellet densities were determined from their masses and volumes and compared with crystallographic densities. Sintered pellets were coated with gold paste which was dried and hardened by heating to ~900 °C and attached with gold foil strips to the Pt leads of a conductivity jig. Impedance measurements were taken at ~50 °C intervals using a Hewlett Packard 4192A analyser, frequency range 5 Hz to 13 MHz and an Agilent 4294 A precision analyser, frequency range 40 Hz to 110 MHz.

DSC was carried out on a Stanton Redcroft thermal analyser, about 0.01 g of a sample was placed in a Pt-crucible and heated to ~700 °C at 10 °C/min, held for 30 min and cooled back to room temperature.

3. Results and discussion

3.1. Ambient temperature structure

XRD results on compositions with $z \leq 1$ showed single phase samples that appeared to be isostructural with $Li_2Mg_2(MoO_4)_3$, for compositions $z > 1.0$, phase mixtures were obtained. All reflections were indexed on a primitive orthorhombic cell with Z=4 and lattice parameters a~5.10, b~10.4 and c~17.6 Å. Unit-cell volume is plotted against composition in Fig. 2. a and V decrease approximately linearly with z, whereas b and c exhibit a non-linear trend. In complex structures, a linear change in lattice parameter, as dictated by Vegard's law, [34] is not always rigorously observed.

The observed systematic absences were consistent with space-group *Pnma* (no. 62) as reported for isostructural double molybdates. XRD and ND data were analysed simultaneously to avoid problems detecting small displacements of weak X-ray scatterers (Li, Mg and O), and from the contrasting neutron scattering lengths of Li and Mg (Li: b=−2.030 fm; Mg: b=5.375 fm) when present in a 3:1 ratio on the same site. The atomic

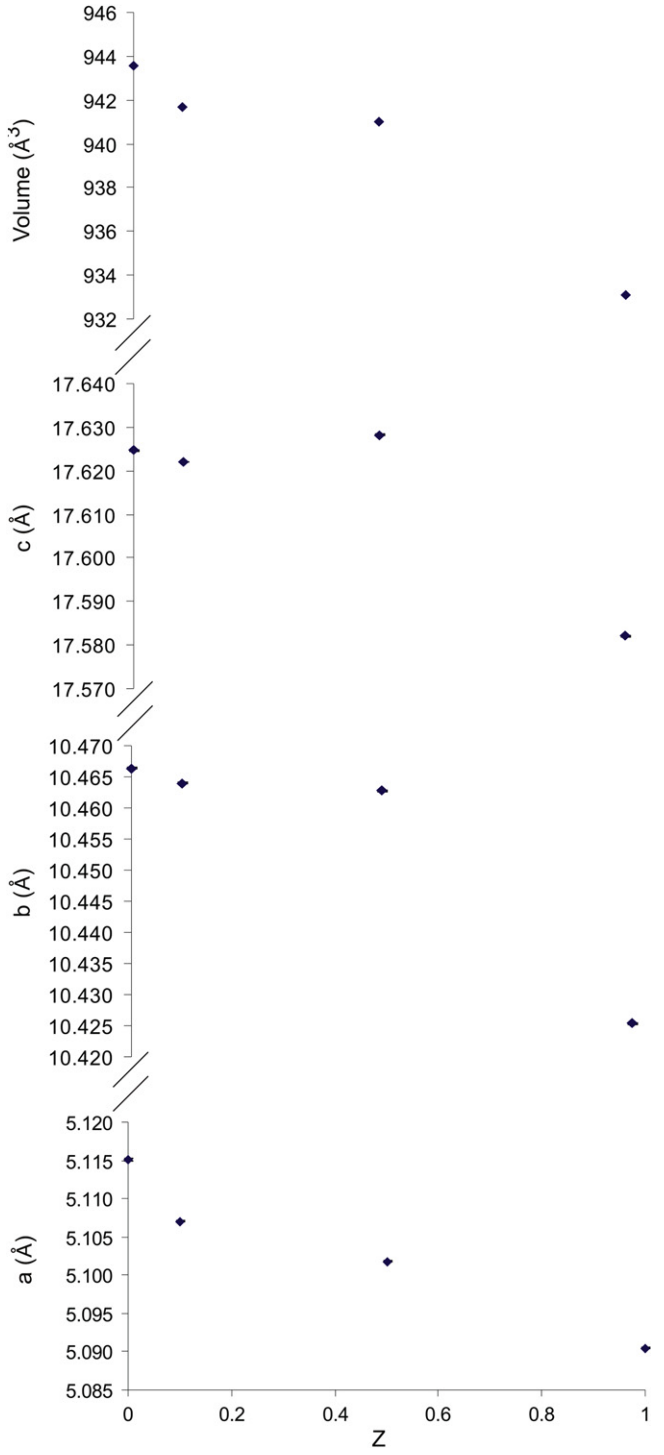

Fig. 2. Evolution of unit-cell parameters and volume with composition, *z*. (Error bars are smaller than the symbols plotted for $z=0$, 0.5 and 1; values taken from Rietveld refinements. For $z=0.1$, errors in lattice parameters determined from peak indexing are 0.005 Å.)

positions of $Li_2Mg_2(MoO_4)_3$ were used as a starting point [15] and *ab initio* methods used to verify the validity of this model. The structure was solved by the introduction of two unique MoO_4 tetrahedra having random positions and orientations with an average Mo–O bond length of 1.775 Å, and as many as four unique Li/Mg positions with variable co-ordinates and occupancies. The new model highlighted some minor atomic displacements and inspection of Fourier maps confirmed the location of the Li/Mg sites, thus providing a more accurate basis for Rietveld refinement. The fractional occupancies of the Li/Mg and V/Mo sites were constrained to ensure 100% occupation, but no constraint was applied regarding the ratio of cations on the different sites. The refinements proceeded smoothly for all samples and converged to give excellent agreement between calculated and experimental profiles, as is illustrated in Figs. 3–5. The corresponding refinement results and principal bond lengths are given in Tables 1–3 with the refined compositions. As the value of *z* increases, the V^{5+} cations are accommodated on the tetrahedral sites and the fractional occupancies of the 6 co-ordinate sites are modified. The fractional occupancies are rationalised below, along with further structural description.

3.1.1. $Li_2Mg_2(MoO_4)_3$; $z=0$

Table 1 summarises the refinement results for $z=0$. These results are in reasonable agreement with previously published single crystal and powder XRD data [15]. Li^+ and Mg^{2+} ions preferentially occupy the trigonal prisms (74% Li^+) and the octahedral sheets (64% Mg^{2+}), respectively, with an almost statistical distribution in the octahedral chains (55% Li^+, 45% Mg^{2+}).

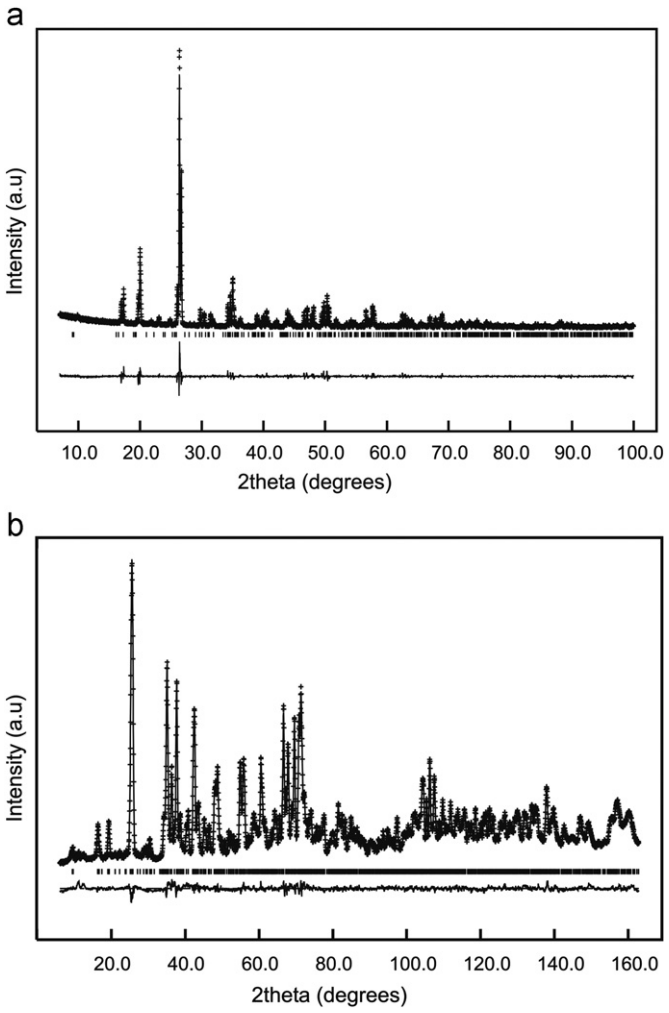

Fig. 3. (a) Calculated (−), experimental (+) and difference (lower horizontal line) profiles from refinement of ambient temperature XRD data for $Li_2Mg_2Mo_3O_{12}$. Vertical tick marks represent allowed Bragg peak positions. (b) Calculated (−), experimental (+) and difference (lower horizontal line) profiles from refinement of ambient temperature ND data for $Li_2Mg_2Mo_3O_{12}$. Vertical tick marks represent allowed Bragg peak positions.

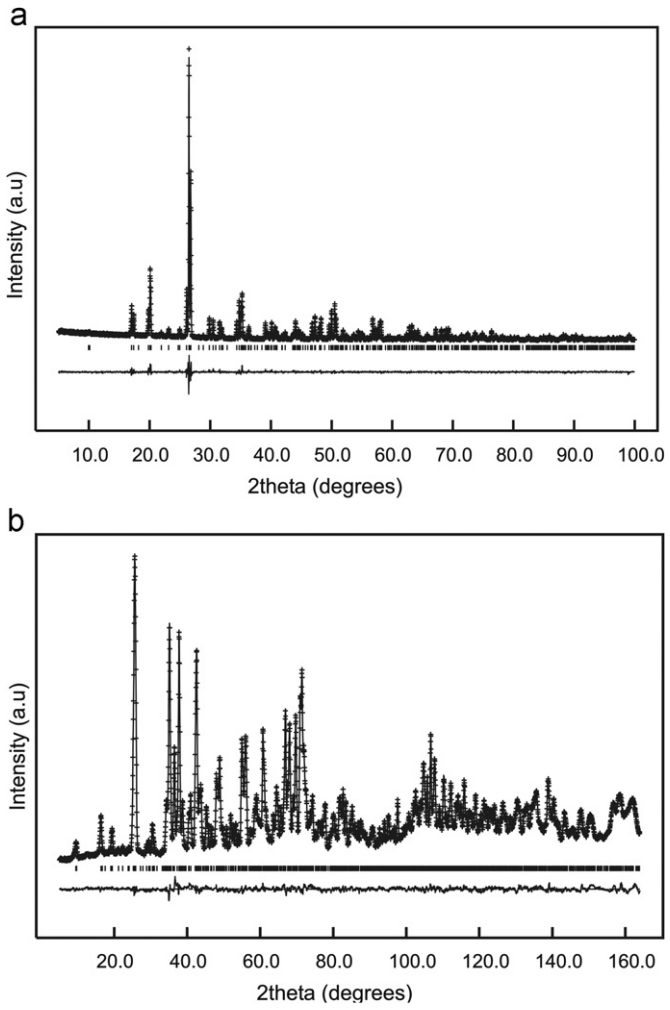

Fig. 4. (a) Calculated (−), experimental (+) and difference (lower horizontal line) profiles from refinement of ambient temperature XRD data for $Li_{1.5}Mg_{2.5}V_{0.5}Mo_{2.5}O_{12}$. Vertical tick marks represent allowed Bragg peak positions. (b) Calculated (−), experimental (+) and difference (lower horizontal line) profiles from refinement of ambient temperature ND data for $Li_{1.5}Mg_{2.5}V_{0.5}Mo_{2.5}O_{12}$. Vertical tick marks represent allowed Bragg peak positions.

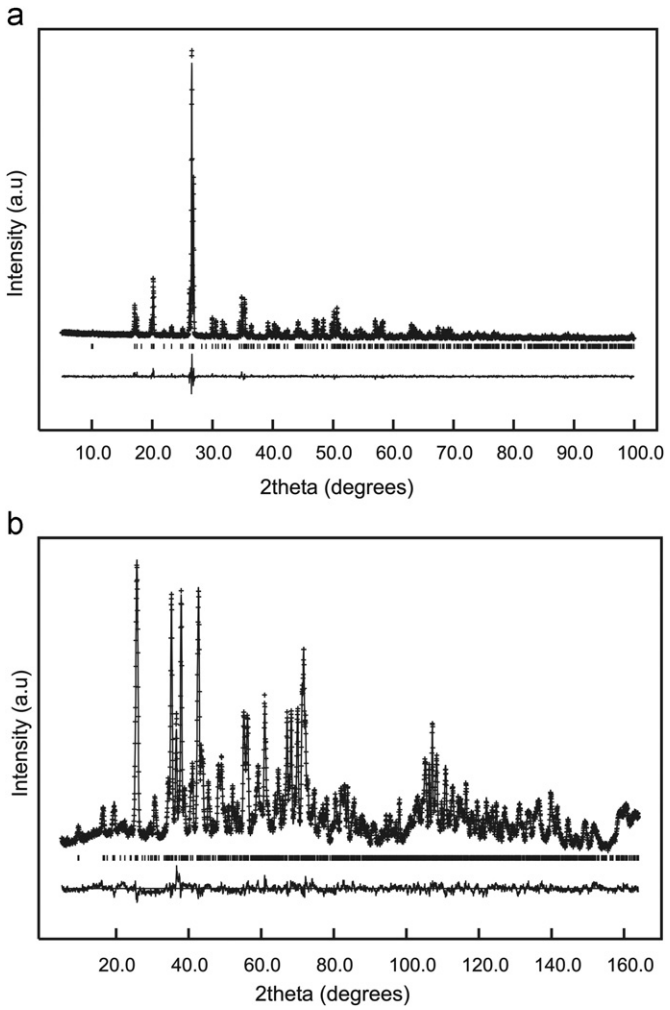

Fig. 5. (a) Calculated (−), experimental (+) and difference (lower horizontal line) profiles from refinement of ambient temperature XRD data for $LiMg_3VMo_2O_{12}$. Vertical tick marks represent allowed Bragg peak positions. (b) Calculated (−), experimental (+) and difference (lower horizontal line) profiles from refinement of ambient temperature ND data for $LiMg_3VMo_2O_{12}$. Vertical tick marks represent allowed Bragg peak positions.

3.1.2. $Li_{1.5}Mg_{2.5}V_{0.5}Mo_{2.5}O_{12}$; $z=0.5$

Table 2 summarises the refinement results for $z=0.5$. Upon substitution with V^{5+}, the Mo/V(2) tetrahedral site is preferentially occupied by the vanadium, whilst a smaller percentage goes onto the Mo/V(1) site. Mo/V(2) is linked to the buckled octahedral sheets and the face-sharing octahedral chains. The excess magnesium, compared with $z=0$, is distributed randomly over all 3 crystallographic sites. The fractional occupancy of site (1) increases from approximately 0.26–0.30 Mg (prisms), from approximately 0.64–0.79 Mg for site (2) (octahedral sheets) and from 0.45 to 0.53 Mg for site (3) (octahedral chains).

3.1.3. $LiMg_3VMo_2O_{12}$; $z=1$

$LiMg_3VMo_2O_{12}$ is a new stoichiometric phase and the refinement results are summarised in Table 3. In contrast to $z=0$ and 0.5, a well-defined 1:3 ratio of Li^+:Mg^{2+} is observed in the face-sharing octahedral chains, whereas the trigonal prisms contain an almost statistical distribution of Li^+ and Mg^{2+}. The V^{5+} cations again preferentially occupy the Mo/V(2) site, perhaps due to the proximity of the octahedral sheets, wherein the excess of Mg^{2+} is located. This may be explained by considering the electrostatic ion–ion repulsions of V^{5+}/Mg^{2+} compared to Mo^{6+}/Mg^{2+}. The tetrahedral sites containing the larger concentration of V^{5+} are linked principally to the magnesium-rich buckled octahedral sheets which may indicate short-range order, or clustering of the Mg^{2+} cations, in close proximity to the VO_4 tetrahedra, in preference to the MoO_4 tetrahedra. Short-range order, or clustering effects, would not be detected by macroscopic crystallographic techniques such as XRD and ND, and would not affect the average structure determination. Short-range ordering of cations is probably the driving force for the precise cation distribution over both 4- and 6-coordinate sites in $z=0.5$ and 1. Table 4 shows the comparison of occupancies across all sites in the series.

3.2. High temperature structure

ND data collected at 650 °C for $z=0$, 0.5 and 1.0 members were refined using the ambient temperature model as a starting point. Extra peaks were observed from the steel canister sample holders which were modelled using the Le Bail profile fitting method in GSAS [35]. No extra reflections or intensity changes related to the molybdate phase were observed and there was no evidence for a significant redistribution of cations over the different crystallographic sites, within 2 estimated standard deviations

Table 1

(a) Refined parameters of $Li_{2-z}Mg_{2+z}V_zMo_{3-z}O_{12}$ ($z=0$) from joint XRD/ND Rietveld refinement at ambient temperature

Atom	Site	*x* (*dx*)	*y* (*dy*)	*z* (*dz*)	$U^{*}_{iso}100$ (Å^2)	Frac.
Mo(1)	8*d*	0.2754(2)	0.5268(1)	0.6567(1)	0.74(2)	1
Mo(2)	4*c*	0.7206(3)	0.75	0.0570(1)	0.74(2)	1
Li/Mg(1)	4*c*	0.2594(1)	0.25	0.2966(1)	0.81(3)	0.735(5)/0.265(5)
Li/Mg(2)	8*d*	0.7527(2)	0.5743(2)	0.5261(2)	0.81(3)	0.359(3)/0.641(3)
Li/Mg(3)	4*c*	0.4008(5)	0.75	0.2521(5)	0.81(3)	0.550(4)/0.450(4)
O(1)	4*c*	0.6422(5)	0.75	0.1539(2)	1.05(1)	1
O(2)	4*c*	0.4397(5)	0.75	0.9942(2)	1.05(1)	1
O(3)	8*d*	0.9154(4)	0.6152(2)	0.0356(1)	1.05(1)	1
O(4)	8*d*	0.0830(4)	0.4893(2)	0.5750(1)	1.05(1)	1
O(5)	8*d*	0.0762(4)	0.6251(2)	0.7137(1)	1.05(1)	1
O(6)	8*d*	0.3511(3)	0.3847(2)	0.7052(1)	1.05(1)	1
O(7)	8*d*	0.5593(4)	0.6130(2)	0.6264(1)	1.05(1)	1

(b) Bond lengths and angles for $Li_{2-z}Mg_{2+z}V_zMo_{3-z}O_{12}$ ($z=0$)

Bond lengths (Å)			Bond angles (deg)		
Mo(1)–O(4)	1.787(2)		O(4)–Mo(1)–O(5)	105.6(1)	
Mo(1)–O(5)	1.763(2)		O(4)–Mo(1)–O(6)	109.1(1)	
Mo(1)–O(6)	1.759(2)		O(4)–Mo(1)-O(7)	108.5(1)	
Mo(1)–O(7)	1.791(2)		O(5)–Mo(1)–O(6)	110.1(1)	
Mo(2)–O(1)	1.754(3)		O(5)–Mo(1)–O(7)	110.2(1)	
Mo(2)–O(2)	1.814(3)		O(6)–Mo(1)–O(7)	113.2(1)	
Mo(2)-O(3)	1.768(2)	(x2)	O(1)–Mo(2)-O(2)	114.4(1)	
			O(1)-Mo(2)–O(3)	109.6(1)	(x2)
			O(2)–Mo(2)–O(3)	108.5(1)	(x2)
			O(3)–Mo(2)–O(3)	105.9(2)	
Li/Mg(1)–O(5)	2.133(10)	(x2)	O(5)–Li/Mg(1)–O(5)	75.6(4)	
Li/Mg(1)–O(5)	2.165(6)	(x2)	O(5)–Li/Mg(1)–O(5)	128.7(8)	(x2)
Li/Mg(1)–O(7)	2.182(13)	(x2)	O(5)-Li/Mg(1)-O(5)	83.4(4)	(x2)
Li/Mg(2)–O(2)	2.103(2)		O(5)-Li/Mg(1)-O(5)	74.3(2)	
Li/Mg(2)–O(3)	2.168(3)		O(5)–Li/Mg(1)–O(7)	131.4(2)	(x2)
Li/Mg(2)–O(3)	2.084(3)		O(5)–Li/Mg(1)–O(7)	81.7(1)	(x2)
Li/Mg(2)-O(4)	2.095(2)		O(5)-Li/Mg(1)-O(7)	89.6(2)	(x2)
Li/Mg(2)–O(4)	2.081(3)		O(5)-Li/Mg(1)-O(7)	141.8(6)	(x2)
Li/Mg(2)–O(7)	2.065(3)		O(7)-Li/Mg(1)-O(7)	82.2(6)	
Li/Mg(3)–O(1)	2.127(6)	(x2)	O(2)–Li/Mg(2)–O(3)	173.3(1)	
Li/Mg(3)–O(6)	2.081(5)	(x2)	O(2)-Li/Mg(2)-O(3)	96.2(1)	
Li/Mg(3)–O(6)	2.040(5)	(x2)	O(2)-Li/Mg(2)-O(4)	94.3(1)	
			O(2)–Li/Mg(2)–O(4)	87.2(1)	
			O(2)–Li/Mg(2)–O(7)	101.1(1)	
			O(3)–Li/Mg(2)–O(3)	84.2(1)	
			O(3)–Li/Mg(2)–O(4)	84.2(1)	
			O(3)-Li/Mg(2)–O(4)	86.2(1)	
			O(3)–Li/Mg(2)–O(4)	165.8(2)	
			O(3)-Li/Mg(2)-O(4)	87.3(1)	
			O(3)-Li/Mg(2)-O(7)	85.6(1)	
			O(3)–Li/Mg(2)–O(7)	90.6(1)	
			O(4)–Li/Mg(2)–O(4)	83.7(1)	
			O(4)–Li/Mg(2)–O(7)	96.8(1)	
			O(4)–Li/Mg(2)-O(7)	171.7(1)	
			O(1)–Li/Mg(3)–O(1)	176.9(4)	
			O(1)–Li/Mg(3)–O(6)	92.1(3)	(x2)
			O(1)–Li/Mg(3)–O(6)	86.5(1)	(x2)
			O(1)–Li/Mg(3)–O(6)	85.6(7)	(x2)
			O(1)–Li/Mg(3)–O(6)	95.8(3)	(x2)
			O(6)–Li/Mg(3)–O(6)	85.3(3)	
			O(6)–Li/Mg(3)–O(6)	178.2(4)	(x2)
			O(6)–Li/Mg(3)–O(6)	93.6(1)	(x2)
			O(6)–Li/Mg(3)–O(6)	87.4(3)	

Space group: *Pnma*, $a=5.11510(5)$ Å; $b=10.46641(9)$ Å; $c=17.62466(16)$ Å.
$\chi^2=2.584$; powder totals $R_{wp}=5.45\%$; $R_p=3.36\%$.
(XRD: $R_{wp}=14.27\%$; $R_p=10.77\%$; $R^2_F=7.75\%$; ND: $R_{wp}=3.42\%$; $R_p=2.59\%$; $R^2_F=3.15\%$).

(esd). Laboratory XRD data collected on samples quenched from high temperature also provided no detectable evidence for a different high temperature structure. Therefore, using bulk structural analysis afforded by diffraction techniques, no detectable evidence for polymorphism was observed.

3.3. Impedance spectroscopy and DSC

Impedance data in the form of a complex plane plot of a representative member, $z=0.5$ of this solid solution series are shown at two temperatures, 482 and 771 °C in Fig. 6, together

Table 2

(a) Refined parameters of $Li_{2-z}Mg_{2+z}V_zMo_{3-z}O_{12}$ ($z=0.5$) from joint XRD/ND Rietveld refinement at ambient temperature

Atom	Site	*x* (*dx*)	*y* (*dy*)	*z* (*dz*)	$U^*_{iso}100$ (Å^2)	Frac.
Mo/V(1)	8*d*	0.27511(5)	0.52740(5)	0.65686(5)	0.53(2)	0.874(1)/0.126(1)
Mo/V(2)	4*c*	0.72179(9)	0.75	0.05631(9)	0.53(2)	0.753(3)/0.247(3)
Li/Mg(1)	4*c*	0.2607(9)	0.25	0.2979(9)	0.98(5)	0.704(3)/0.296(3)
Li/Mg(2)	8*d*	0.75367(9)	0.57527(9)	0.52707(9)	0.98(5)	0.214(3)/0.786(3)
Li/Mg(3)	4*c*	0.3994(3)	0.75	0.2507(3)	0.98(5)	0.465(4)/0.535(4)
O(1)	4*c*	0.6430(4)	0.75	0.1523(1)	1.28(1)	1
O(2)	4*c*	0.4395(4)	0.75	0.9946(1)	1.28(1)	1
O(3)	8*d*	0.9161(3)	0.6157(2)	0.0354(1)	1.28(1)	1
O(4)	8*d*	0.0837(3)	0.4918(1)	0.5747(1)	1.28(1)	1
O(5)	8*d*	0.0777(3)	0.6252(1)	0.7136(1)	1.28(1)	1
O(6)	8*d*	0.3507(3)	0.3855(2)	0.7052(1)	1.28(1)	1
O(7)	8*d*	0.5618(3)	0.6133(1)	0.6267(1)	1.28(1)	1

(b) Bond lengths and angles for $Li_{2-z}Mg_{2+z}V_zMo_{3-z}O_{12}$ ($z=0.5$)

Bond lengths (Å)			Bond angles (deg)		
Mo/V(1)–O(4)	1.787(2)		O(4)–Mo/V(1)–O(5)	105.72(7)	
Mo/V(1)–O(5)	1.750(2)		O(4)–Mo/V(1)–O(6)	109.74(8)	
Mo/V(1)–O(6)	1.755(2)		O(4)–Mo/V(1)–O(7)	107.99(8)	
Mo/V(1)–O(7)	1.798(2)		O(5)–Mo/V(1)–O(6)	110.09(8)	
Mo/V(2)–O(1)	1.739(3)		O(5)–Mo/V(1)–O(7)	110.19(8)	
Mo/V(2)–O(2)	1.804(3)		O(6)–Mo/V(1)–O(7)	112.85(6)	
Mo/V(2)–O(3)	1.759(2)	(x2)	O(1)–Mo/V(2)–O(2)	113.7(1)	
			O(1)–Mo/V(2)–O(3)	109.51(9)	(x2)
			O(2)–Mo/V(2)–O(3)	108.9(1)	(x2)
			O(3)–Mo/V(2)–O(3)	106.1(1)	
Li/Mg(1)–O(5)	2.142(9)	(x2)	O(5)–Li/Mg(1)–O(5)	75.1(4)	
Li/Mg(1)–O(5)	2.174(5)	(x2)	O(5)–Li/Mg(1)–O(5)	127.4(8)	(x2)
Li/Mg(1)–O(7)	2.153(12)	(x2)	O(5)–Li/Mg(1)–O(5)	82.8(3)	(x2)
Li/Mg(2)–O(2)	2.095(1)		O(5)–Li/Mg(1)–O(5)	73.8(2)	
Li/Mg(2)–O(3)	2.182(2)		O(5)–Li/Mg(1)–O(7)	132.2(2)	(x2)
Li/Mg(2)–O(3)	2.088(2)		O(5)–Li/Mg(1)–O(7)	82.1(1)	(x2)
Li/Mg(2)–O(4)	2.074(2)		O(5)–Li/Mg(1)–O(7)	89.6(2)	(x2)
Li/Mg(2)–O(4)	2.097(2)		O(5)–Li/Mg(1)–O(7)	142.2(5)	(x2)
Li/Mg(2)–O(7)	2.049(2)		O(7)–Li/Mg(1)–O(7)	83.2(6)	
Li/Mg(3)–O(1)	2.134(4)		O(2)–Li/Mg(2)–O(3)	172.3(1)	
Li/Mg(3)–O(1)	2.153(4)		O(2)–Li/Mg(2)–O(3)	95.76(8)	
Li/Mg(3)–O(6)	2.068(3)	(x2)	O(2)–Li/Mg(2)–O(4)	94.24(8)	
Li/Mg(3)–O(6)	2.059(3)	(x2)	O(2)–Li/Mg(2)–O(4)	87.52(7)	
			O(2)–Li/Mg(2)–O(7)	101.7(1)	
			O(3)–Li/Mg(2)–O(3)	83.89(8)	
			O(3)–Li/Mg(2)–O(4)	84.81(6)	
			O(3)–Li/Mg(2)–O(4)	84.73(8)	
			O(3)–Li/Mg(2)–O(4)	165.6(1)	
			O(3)–Li/Mg(2)–O(4)	86.7(1)	
			O(3)–Li/Mg(2)–O(7)	86.02(6)	
			O(3)–Li/Mg(2)–O(7)	91.07(6)	
			O(4)–Li/Mg(2)–O(4)	83.32(7)	
			O(4)–Li/Mg(2)–O(7)	97.07(9)	
			O(4)–Li/Mg(2)–O(7)	170.67(8)	
			O(1)–Li/Mg(3)–O(1)	178.2(3)	
			O(1)–Li/Mg(3)–O(6)	92.6(2)	(x2)
			O(1)–Li/Mg(3)–O(6)	86.9(1)	(x2)
			O(1)–Li/Mg(3)–O(6)	86.2(1)	(x2)
			O(1)–Li/Mg(3)–O(6)	94.4(2)	(x2)
			O(6)–Li/Mg(3)–O(6)	86.5(2)	
			O(6)–Li/Mg(3)–O(6)	179.40(1)	(x2)
			O(6)–Li/Mg(3)–O(6)	93.25(8)	(x2)
			O(6)–Li/Mg(3)–O(6)	87.0(2)	

Space group: *Pnma*, $a=5.10182(6)$ Å; $b=10.46275(12)$ Å; $c=17.62825(20)$ Å.
$\chi^2=2.473$; powder totals $R_{wp}=3.50\%$; $R_p=2.47\%$.
(XRD: $R_{wp}=8.20\%$; $R_p=6.31\%$; $R_F^2=7.12\%$; ND: $R_{wp}=2.70\%$; $R_p=2.13\%$; $R_F^2=3.05\%$).

with combined "M/Z" spectroscopic plots at 482 °C. The impedance data show a single essentially undistorted semi-circle (a) with associated capacitance ~8 pF and a low frequency arc or inclined spike (b) with associated capacitance ~29 μF. The latter value is typical of a double-layer capacitance associated with blocking electrodes and is therefore taken as good evidence that the material is a conductor of Li^+ ions. The M''/Z'' plot shown in (c) uses the same data as shown in (a) for the complex plane plot and the occurrence of a single coincident peak in the two spectra indicates that the response of the sample can be represented by a single parallel RC element; further, from the magnitude of the capacitance, this represents the bulk response of the sample and

Table 3

(a) Refined parameters of $Li_{2-z}Mg_{2+z}V_zMo_{3-z}O_{12}$ ($z=1$) from joint XRD/ND Rietveld refinement at ambient temperature

Atom	Site	*x* (*dx*)	*y* (*dy*)	*z* (*dz*)	$U^*_{iso}100$ (Å^2)	Frac.
Mo/V(1)	8*d*	0.27513(7)	0.52742(7)	0.65688(7)	0.97(4)	0.718(2)/0.282(1)
Mo/V(2)	4*c*	0.7216(1)	0.75	0.0561(1)	0.97(4)	0.564(4)/0.436(4)
Li/Mg(1)	4*c*	0.2624(6)	0.25	0.29796(6)	1.50(5)	0.530(5)/0.470(5)
Li/Mg(2)	8*d*	0.7539(3)	0.5755(1)	0.5273(1)	1.50(5)	0.110(2)/0.890(2)
Li/Mg(3)	4*c*	0.4001(3)	0.75	0.2514(3)	1.50(5)	0.25/0.75
O(1)	4*c*	0.6436(7)	0.75	0.1526(2)	1.23(2)	1
O(2)	4*c*	0.4397(7)	0.75	0.9938(2)	1.23(2)	1
O(3)	8*d*	0.9146(5)	0.6171(2)	0.0343(1)	1.23(2)	1
O(4)	8*d*	0.0854(5)	0.4926(2)	0.5749(1)	1.23(2)	1
O(5)	8*d*	0.0764(5)	0.6256(2)	0.7053(2)	1.23(2)	1
O(6)	8*d*	0.3506(4)	0.3872(2)	0.70532(2)	1.23(2)	1
O(7)	8*d*	0.5630(5)	0.6139(2)	0.6267(1)	1.23(2)	1

(b) Bond lengths and angles for $Li_{2-z}Mg_{2+z}V_zMo_{3-z}O_{12}$ ($z=1$)

Bond lengths (Å)			Bond angles (deg)		
Mo/V(1)–O(4)	1.773(3)		O(4)–Mo/V(1)–O(5)	105.7 (1)	
Mo/V(1)–O(5)	1.755(3)		O(4)–Mo/V(1)–O(6)	110.3(1)	
Mo/V(1)–O(6)	1.735(2)		O(4)–Mo/V(1)–O(7)	107.8(1)	
Mo/V(1)–O(7)	1.800(3)		O(5)–Mo/V(1)–O(6)	109.8(1)	
Mo/V(2)–O(1)	1.742(4)		O(5)–Mo/V(1)–O(7)	110.2(1)	
Mo/V(2)–O(2)	1.806(4)		O(6)–Mo/V(1)–O(7)	112.7(1)	
Mo/V(2)–O(3)	1.741(3)	(x2)	O(1)–Mo/V(2)–O(2)	114.2(2)	
			O(1)–Mo/V(2)–O(3)	110.0(1)	(x2)
			O(2)–Mo/V(2)–O(3)	108.4(2)	(x2)
			O(3)–Mo/V(2)–O(3)	105.5(2)	
Li/Mg(1)–O(5)	2.150(6)	(x2)	O(5)–Li/Mg(1)–O(5)	74.2(3)	
Li/Mg(1)–O(5)	2.171(4)	(x2)	O(5)–Li/Mg(1)–O(5)	125.9(5)	(x2)
Li/Mg(1)–O(7)	2.118(8)	(x2)	O(5)–Li/Mg(1)–O(5)	82.3(2)	(x2)
Li/Mg(2)–O(2)	2.084(2)		O(5)–Li/Mg(1)–O(5)	73.8(2)	
Li/Mg(2)–O(3)	2.186(3)		O(5)–Li/Mg(1)–O(7)	132.3(1)	(x2)
Li/Mg(2)–O(3)	2.084(3)		O(5)–Li/Mg(1)–O(7)	82.2(1)	(x2)
Li/Mg(2)–O(4)	2.073(3)		O(5)–Li/Mg(1)–O(7)	90.0(1)	(x2)
Li/Mg(2)–O(4)	2.097(3)		O(5)–Li/Mg(1)–O(7)	143.2(3)	(x2)
Li/Mg(2)–O(7)	2.040(3)		O(7)–Li/Mg(1)–O(7)	84.1(4)	
Li/Mg(3)–O(1)	2.134(5)		O(2)–Li/Mg(2)–O(3)	171.8(2)	
Li/Mg(3)–O(1)	2.135(5)		O(2)–Li/Mg(2)–O(3)	95.9(1)	
Li/Mg(3)–O(6)	2.081(4)	(x2)	O(2)–Li/Mg(2)–O(4)	93.8(1)	
Li/Mg(3)–O(6)	2.059(3)	(x2)	O(2)–Li/Mg(2)–O(4)	88.1(1)	
			O(2)–Li/Mg(2)–O(7)	101.4(1)	
			O(3)–Li/Mg(2)–O(3)	84.0(1)	
			O(3)–Li/Mg(2)–O(4)	85.0(1)	
			O(3)–Li/Mg(2)–O(4)	83.8(1)	
			O(3)–Li/Mg(2)–O(4)	166.3(2)	
			O(3)–Li/Mg(2)–O(4)	87.1(1)	
			O(3)–Li/Mg(2)–O(7)	86.8(1)	
			O(3)–Li/Mg(2)–O(7)	90.6(1)	
			O(4)–Li/Mg(2)–O(4)	83.5(1)	
			O(4)–Li/Mg(2)–O(7)	97.1(1)	
			O(4)–Li/Mg(2)–O(7)	170.5(1)	
			O(1)–Li/Mg(3)–O(1)	177.8(3)	
			O(1)–Li/Mg(3)–O(6)	92.3(2)	(x2)
			O(1)–Li/Mg(3)–O(6)	86.7(1)	(x2)
			O(1)–Li/Mg(3)–O(6)	86.2(1)	(x2)
			O(1)–Li/Mg(3)–O(6)	94.8(2)	(x2)
			O(6)–Li/Mg(3)–O(6)	86.8(2)	
			O(6)–Li/Mg(3)–O(6)	178.8(3)	(x2)
			O(6)–Li/Mg(3)–O(6)	92.6(1)	(x2)
			O(6)–Li/Mg(3)–O(6)	88.0(2)	

Space group: *Pnma*, $a=5.09044(6)$ Å; $b=10.42539(10)$ Å; $c=17.58204(19)$ Å.
$\chi^2=2.220$; powder totals $R_{wp}=3.42\%$; $R_p=2.35\%$.
(XRD: $R_{wp}=9.72\%$; $R_p=7.47\%$; $R_F^2=7.73\%$; ND: $R_{wp}=2.56\%$; $R_p=2.03\%$; $R_F^2=5.34\%$).

Table 4
Cation distribution of $Li_{2-z}Mg_{2+z}V_zMo_{3-z}O_{12}$ solid solution members.

z	M(1)—prisms	M(2)—oct. sheets	M(3)—oct. chains	Mo/V(1)—tet.	Mo/V(2)—tet.
0	74% Li:26% Mg	36% Li:64% Mg	55% Li:45% Mg	100% Mo	100% Mo
0.5	70% Li:30% Mg	21% Li:79% Mg	47% Li:53% Mg	87% Mo:13% V	75% Mo:25% V
1	53% Li:47% Mg	11% Li:89% Mg	25% Li:75% Mg	72% Mo:28% V	56% Mo:44% V

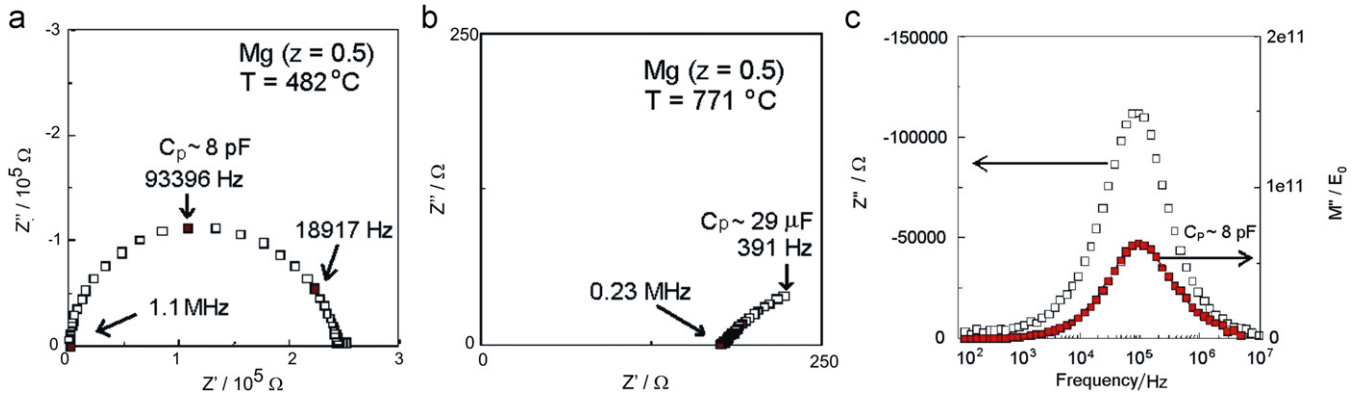

Fig. 6. Impedance spectrum of $z=0.5$ measured at (a) $T=482$ °C, (b) $T=771$ °C, (c) Combined M''/Z'' and spectroscopic plot at $T=482$ °C.

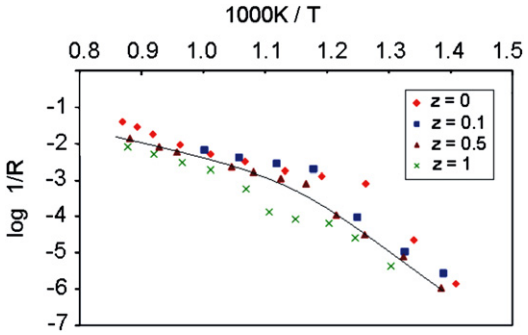

Fig. 7. Arrhenius plot of conductivity data showing change in slope with z. (A line is drawn for $z=0.5$ as a guideline for the eye to demonstrate the curvature of the data.)

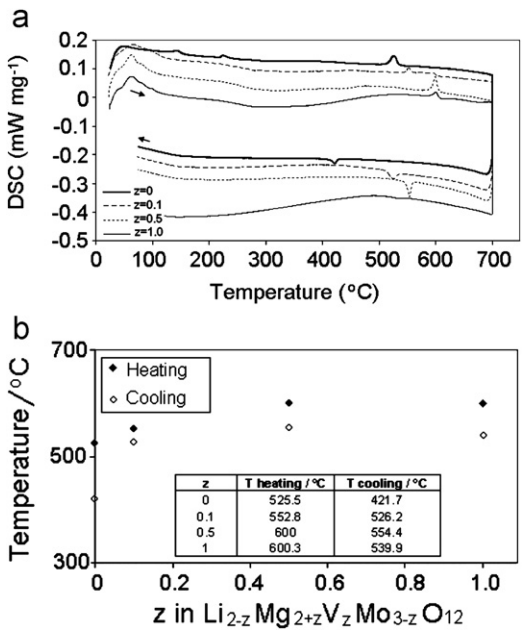

Fig. 8. (a) DSC data for $Li_{2-z}Mg_{2+z}V_zMo_{3-z}O_{12}$ $(0 \le z \le 1)$ during heating and cooling cycles. (b) Evolution of transition temperature with z.

therefore, the low frequency intercept of the arc on the complex plane plot can be taken as sample bulk resistance.

Conductivity data obtained from plots as shown in (a) are plotted against reciprocal temperature in Arrhenius format, Fig. 7. Data are shown for four compositions (including $z=0.1$ which was isostructural with other solid solution members), all of which show a change in slope, the temperature of the transition increasing with increasing value of z. For $z=0$, the transition is quite sharp, it remains fairly sharp for $z=0.1$ but then becomes much broader for $z=0.5$. To either side of the transition, the conductivity Arrhenius plots show some evidence of curvature and therefore values of activation energies are only approximate. To test whether the changes in the Arrhenius plots were associated with a phase transition, DSC data were recorded on heating and cooling cycles. Results are summarised in Fig. 8a and b and show an approximate correlation between the peak temperature seen by DSC and the changes of slope in the conductivity plot.

From the nature of the blocking electrode capacitance seen in the impedance complex plane plots (Fig. 6b) it is clear that the principal conduction mechanism is by Li^+ ions. At high temperatures, above 500–600 °C depending on composition, the materials are reasonably good Li^+ ion conductors with conductivities $\geq 10^{-3}$ S cm^{-1} and the activation energies, ~0.6–0.8 eV, are also consistent with Li^+ ion conductivity. Below 500–600 °C, the activation energies are much greater, consistent with structures in which Li^+ ions are probably ordered with little mobility. The phase transitions at 500–600 °C are thermodynamically first order, as shown by the occurrence of transition enthalpies in the DSC data and therefore indicate a structural transition from ordered to mobile Li^+ ions in at least part of the structures. From the high temperature ND data, there was no obvious difference between the structures of the ambient and high temperature polymorphs and therefore small changes in lithium site distributions and occupancies are thought to be responsible. At all temperatures, the lithium ion conductivity is highest for composition $z=0$, decreases with decreasing Li content and has the smallest set of values for the composition $LiMg_3VMo_2O_{12}$. This is also consistent with the crystallographic results demonstrating preferential order of Li and Mg in the octahedral chains.

4. Conclusions

A new vanado-molybdate phase $LiMg_3VMo_2O_{12}$ and the $z=0.5$ member of the solid solution $Li_{2-z}Mg_{2+z}V_zMo_{3-z}O_{12}$ have been synthesized and characterized. Combined Rietveld refinement of laboratory XRD and high resolution ND data have been used to determine the crystal structures of these compounds. Preferential occupation of the distinct crystallographic sites is observed for all 4 cations. Li^+ cations show a strong preference for the trigonal prismatic sites and extra Mg^{2+} is accommodated first in the buckled octahedral sheets and face-sharing octahedral sites before being substituted into the prisms. V^{5+} cations initially substitute into sites adjacent to the buckled octahedral layers, but as the concentration increases, a more statistical partitioning is observed. Conductivity data show a change in the slope of the

Arrhenius plots and this can be correlated to a structural transition, evidenced by DSC, at higher temperatures. However, by diffraction techniques, no detectable change in the structure is observed, leading to the conclusion that no bulk long-range reorganisation of the structure is occurring during this transition, and therefore its nature is still unclear.

Acknowledgments

The authors gratefully acknowledge the University of Sheffield and the EPSRC sponsored portfolio partnership award "Advanced Ceramics and Composites," for the provision of a studentship and fellowship respectively for SDS and LJG. This research project has been supported by the European Commission under the 6th Framework Programme through the Key Action: Strengthening the European Research Area, Research Infrastructures. Contract no. RII3-CT-2003-505925, and is based on experiments performed at the Swiss spallation neutron source SINQ, Paul Scherrer Institute, Villigen, Switzerland.

References

[1] J.D. Pless, B.B. Bardin, H.-S. Kim, D. Ko, M.T. Smith, R.R. Hammond, P.C. Stair, K.R. Poeppelmeier, J. Catal. 223 (1981) 419.
[2] M.A. Chaar, D. Patel, M.C. Kung, H.H. Kung, J. Catal. 105 (1987) 483.
[3] W.D. Harding, H.H. Kung, V.L. Kozhevnikov, K.R. Poeppelmeier, J. Catal. 144 (1993) 597.
[4] O.S. Owen, H.H. Kung, J. Mol. Catal. 79 (1993) 265.
[5] V.G. Zubkov, I.A. Leonidov, K.R. Poeppelmeier, V.L. Kozhevnikov, J. Solid State Chem. 111 (1994) 197.
[6] X. Wang, J.D. Pless, D.A. Vander Griend, P.C. Stair, K.R. Poeppelmeier, Z. Hu, J.D. Jorgensen, J. Alloys Compd. 379 (2004) 87.
[7] N. Krishnamachari, C. Calvo, Can. J. Chem. 49 (1971) 1629.
[8] C. Gicquel, M. Mayer, G. Perez, R. Bouaziz, C.R. Acad. Sci. C275 (1972) 265.
[9] M. Ozima, S. Sato, T. Zoltai, Acta Crystallogr. B33 (1977) 2175.
[10] P.V. Klevtsov, V.G. Kim, R.F. Klevtsova, Sov. Phys. Crystallogr. 25 (1980) 175.
[11] C. Gicquel-Mayer, M. Mayer, G. Perez, Acta Crystallogr. B37 (1981) 1035.
[12] S.F. Solodovnikov, Z.A. Solodovnikova, R.F. Klevtsova, L.A. Glinskaya, P.V. Klevtsov, E.S. Zolotova, J. Struct. Chem. 35 (1994) 871.
[13] V.A. Efremov, Yu.A. Velikhodnyi, V.K. Trunov, Kristallografiya 20 (1975) 287.
[14] V.A. Efremov, V.K. Trunov, Zh. Neorg. Khim. 17 (1972) 2034.
[15] L. Sebastian, Y. Piffard, A.K. Shukla, F. Taulelle, J. Gopalakrishnan, J. Mater. Chem. 13 (2003) 1797.
[16] J.A. Ibers, G.W. Smith, Acta Crystallogr. 17 (1964) 190.
[17] R.F. Klevtsova, S.A. Magarill, Kristallografiya 15 (1970) 710.
[18] M. Wiesmann, H. Svoboda, H. Weitzel, H. Fuess, Z. Krist 210 (1995) 525.
[19] J.P. Smit, P.C. Stair, K.R. Poeppelmeier, Chem. Eur. J. (2006) 5944.
[20] H.Y-P. Hong, Mater. Res. Bull. 11 (1976) 173.
[21] J. Alamo, R. Roy, J. Mater. Sci. 21 (1986) 444.
[22] A. Manthiram, J.B. Goodenough, J. Power Sources 26 (1989) 403.
[23] A. Nadiri, C. Delmas, R. Salmon, P. Hagenmuller, Rév. Chim. Minér. 21 (1984) 537.
[24] C.C. Torardi, E. Prince, Mater. Res. Bull. 21 (1986) 719.
[25] G.T.K. Fey, W. Li, J.R. Dahn, J. Electrochem. Soc. 141 (1994) 2279.
[26] M. Kurzawa, M. Bosacka, P. Jakubus, J. Mater. Sci. 38 (2003) 3137.
[27] A.K. Ivanov-Shits, A.V. Nistyuk, N.G. Chaban, Inorg. Mater. 35 (1999) 756.
[28] A.I. Korosteleva, V.I. Kovalenko, E.A. Ukshe, Neorg. Mater. 17 (1981) 748.
[29] K.M. Begam, M.S. Michael, Y.H. Taufiq-Yap, S.R.S. Prabaharan, Electrochem. Solid State Lett. 7 (2004) A242.
[30] S.R.S. Prabaharan, S. Ramesh, M.S. Michael, K.M. Begam, Mater. Chem. Phys. 87 (2004) 318.
[31] JCPDS—Joint Committee of Powder Diffraction Standards, International Centre for Diffraction Data, USA, 2001.
[32] V. Favre-Nicolin, R. Černý, J. Appl. Crystallogr. 35 (2002) 734.
[33] A.C. Larson, R.B. Von Dreele, General Structure Analysis System (GSAS), Los Alamos National Laboratory Report LAUR 86-748, 1994.
[34] L. Vegard, H. Dale, Z. Krist 67 (1928) 148.
[35] A. Le Bail, H. Duroy, J.L. Fourquet, Mater. Res. Bull. 23 (1988) 447.